Impacts of model resolution on simulation of meso-scale eddies in the Northeast Pacific Ocean

Youyu Lu[1]*, Jiaxing Li[2], Ji Lei[3] and Charles Hannah[4]

[1] Ocean and Ecosystem Sciences Division, Bedford Institute of Oceanography, Fisheries and Oceans Canada, Dartmouth, Nova Scotia, Canada

[2] College of Marine Science and Engineering, Tianjin University of Science and Technology, TEDA, Tianjin, China

[3] Meteorological Research Division, Environment and Climate Change Canada, Dorval, Quebec, Canada

[4] Institute of Ocean Sciences, Fisheries and Oceans Canada, Sidney, British Columbia, Canada

Abstract: The model simulated meso-scale eddies in the Northeast Pacific Ocean, using two models with nominal horizontal resolutions of $1/12°$ and $1/36°$ in latitude/longitude (grid spacing of 7.5 km and 2.5 km), respectively, are presented. Compared with the $1/12°$ model, the $1/36°$ model obtains (1) similar variance and wave number spectra of the sea level anomaly and water temperature anomaly, and (2) increases in the level of the domain-averaged total kinetic energy, eddy kinetic energy (EKE), and variance of horizontal gradient of water temperature. In the interior basin of the southern region, both models show stronger eddy frontal activities, represented by EKE, temperature and its horizontal gradient, in summer and fall than in winter and spring. The challenge of evaluating the realism of high-resolution ocean models with conventional satellite remote sensing observations is discussed.

Keywords: meso-scale eddies; Northeast Pacific Ocean; ocean modelling

*Correspondence to: Youyu Lu, Ocean and Ecosystem Sciences Division, Bedford Institute of Oceanography, Fisheries and Oceans Canada, 1 Challenger Drive, Dartmouth, Nova Scotia, B2Y 4A2, Canada; Email: Youyu.Lu@dfo-mpo.gc.ca

1. Introduction

The rapid increase in computer power has enabled increases in the spatial resolution of ocean models for research and operational applications. With horizontal resolution of about 10 km, models are able to resolve the first mode of the baroclinic Rossby radius of deformation in regions with strong stratification, and hence simulate energetic meso-scale eddy variations (*e.g*., Smith *et al.*, 2000; Delworth *et al.*, 2012). While it has been demonstrated that further increase of horizontal resolution to less than 1 km can resolve sub-meso scale variations, it is less clear about the benefit of model simulations with horizontal grid spacing of a few kilometers. In shelf and coastal waters, one may argue that any increase in resolution can lead to simulation of finer spatial variations due to better representation of bathymetry and coastlines that

steer ocean currents. In the deep ocean, however, the primary question to answer is whether the models better simulate the energetics of meso-scale eddies generated by baroclinic and barotropic instabilities.

Recently, two ocean models with a nominal horizontal resolution of 1/36 in latitude/longitude (corresponding to grid spacing of about 2.5 km), denoted as GoMSS and GBN36, respectively, have been developed by Canadian research groups for regions in the western North Atlantic. GoMSS covers the Gulf of Maine and Scotian Shelf region. It simulates fine spatial scale structure of the seasonal hydrography and circulation, as well as the influence of stratification on tides represented by a striation pattern of alternating highs and lows in the M2 surface summer maximum speed in the Gulf of Maine (Katavouta *et al.*, 2016). GBN36 covers the region around the Grand Banks of Newfoundland (Zhai *et al.*, 2015). Compared

with the solution of a model covering the North Atlantic and Arctic Oceans with a nominal horizontal resolution of 1/12 (CREG12; Dupont *et al.*, 2015), GBN36 obtains increased eddy kinetic energy (EKE) and decreased mean kinetic energy (MKE). GBN36 obtains the MKE of surface geostrophic currents and total currents similar to that derived from mean dynamic topography (MDT) and drifter data, whereas CREG12 overestimates these quantities by 40%−50%. CREG12 and GBN36 underestimate the EKE of surface geostrophic currents by 45% and 30%, respectively, with respect to the EKE derived from along-track altimeter data. Both GBN36 and CREG12 obtain wavenumber spectra of sea level anomaly in close agreement with the spectrum derived from along-track altimeter data, with a slope of −5 at wavelengths near 100 km on logarithmic spectral density scales.

The study of area of Zhai *et al.* (2015) presents strong meso-scale eddies generated by instabilities associated with the confluence of strong western boundary currents, *i.e.*, the cold and fresh Labrador Current from north, and the warm and salty North Atlantic Current from the southwest. In this study, we examine the impacts of model resolution on the simulation of meso-scale eddies in the Northeast Pacific Ocean, an eastern boundary current system with much weaker mean currents than the northwest Atlantic. For this purpose, we develop two ocean models, with nominal horizontal resolutions of $1/12°$ and $1/36°$, respectively. The evaluation of model solutions makes use of available satellite altimeter observations of sea surface height and surface geostrophic currents, but the analysis extends to variations in the horizontal gradient of ocean temperature. The models are introduced in Section 2. The analysis results are presented in Section 3. Conclusion and discussions of results are provided in Section 4.

2. Description of Models

Two models are developed for this study based on the ocean component named the Océan Parallélisé System (OPA; Madec *et al.*, 1998; Madec, 2008) adopted in version 3.1 of the Nucleus European Modelling of the Ocean (NEMO; https://www.nemo-ocean.eu). The sea-ice component is turned off and the minimum sea surface temperature (SST) is set to be the freezing temperature.

Figure 1 shows the domains of the two models. The outer model has a nominal horizontal resolution of $1/12°$. It is intended for the expansion of the CREG12 model described by Dupont *et al.* (2015) to the subpolar North Pacific, hence is still referred to as CREG12 in this paper. It covers roughly from $42°N$ to Bering Strait. The inner model covers the Northeast Pacific Ocean with a nominal horizontal resolution of $1/36°$, hence referred to as NEP36. The grids of both models follow the tri-polar ORCA configuration (Drakkar Group, 2007). The bathymetry of CREG12 configuration is taken from that used in the ORCA12-T321 run of Mercator Océan, France. It is based on ETOPO2 (http://www.ngdc.noaa.gov/mgg/global, Amante and Eakins, 2009). The minimum depth is set at 20 m. The bathymetry of NEP36 is the block-median of SRTM30_Plus, the global bathymetry and elevation data at 30 arc-second resolution (Becker *et al.*, 2009), and with significant modification and tuning. The modifications are based on bathymetry data used by a number of high-resolution unstructured-grid models developed for shelf seas off west coast of Canada. The tuning is primarily modifications of the model's coastline data to improve the simulation of major constituents of tides. The two models use the same set up of vertical grid, with 50 z-levels in full cell sizes in the water column and partial cells near the bottom. The full cell sizes vary from 1 m at the surface to 450 m at 5000 m. There are 23, 27 and 32 levels for the upper 100 m, 200 m and 500 m, respectively.
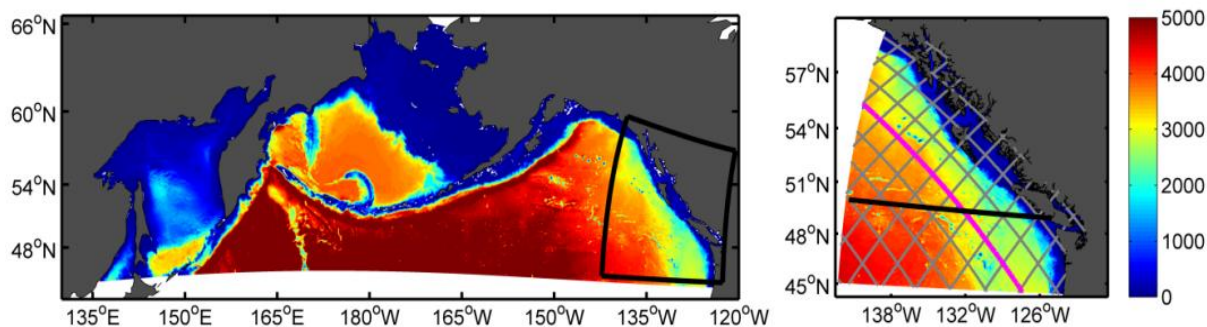

Figure 1. Left panel: Bottom topography (color shading) and domains of the CREG012 (whole color shaded area) and NEP036 (box outlined by black lines). Right panel: Bottom topography (color shading) and domain of NEP036, overlaid JASON-1 satellite altimeter ground tracks (gray lines) with the one in bold pink being used for sea level spectral analysis. The bold black line denotes the section for analysis of temperature gradient. The color axis on the right applies to topography of both panels.

Both models are initialized on January 1, 2003, using the monthly mean temperature and salinity (T-S) of January 2003 from a global ocean reanalysis product, namely GLORYS 2v1 produced by Mercator-Ocean, France (Ferry *et al.*, 2012). The "one-way nested" approach is adopted to set up the lateral open boundary condition for T, S, sea surface height (SSH) and non-tidal velocities. For CREG12, the above fields at the lateral open boundaries are obtained by linearly interpolating the monthly fields of GLORYS 2v1on the CREG12 grid. For NEP36, the above fields are obtained by linearly interpolating the 5-day averaged fields of CREG12. In both models, the inclusion of tidal forcing of 5 constituents (K1, O1, M2, S2 and N2) at the lateral open boundaries has been tested and reasonable solutions are obtained. In particular, the simulation of tides has guided the modification of bathymetry and coastline of NEP36. However, with a focus on meso-scale eddies in the interior basin, this study is based on the solutions of the two models without including tides.

At the open boundaries, the barotropic (depth-averaged) and the baroclinic components of horizontal velocities are treated differently. The radiation condition of Flather (1976) is applied to the barotropic velocity normal to a lateral open boundary. The barotropic velocity tangential to the boundary and SSH are set to be the prescribed values. For the baroclinic velocity in both normal and tangential directions, the Orlanski forward implicit condition (Marchesiello *et al.*, 2001) is applied. Additional nudging of the baroclinic velocity, T and S, to the prescribed values, is applied within a relaxation band inside the lateral open boundaries. The band is 10-grid spacing wide, and the nudging strength decreases from 1 day^{-1} right at the boundary to zero at the 10th grid-layer inside the lateral boundary.

At the ocean surface, the models are forced by hourly atmospheric forcing, taken from an historical re-forecast from the operational Global Deterministic Prediction System of the Canadian Meteorological Centre (Smith *et al.*, 2014). This re-forecast has a horizontal resolution of 33 km at 60 °N.

Finally, the models include the parameterizations of turbulent mixing. Vertical eddy diffusivity and viscosity uses a 1.5 turbulence closure scheme (Gaspar *et al.*, 1990; Blanke and Delecluse, 1993; Mellor and Blumberg, 2004; Axell, 2002). A scale-selective bi-harmonic operator is used to parameterize the horizontal mixing of moment. The viscosity varies spatially with the cube of the horizontal grid spacing according to $-A_M (\Delta x/\Delta x_m)^3$, where A_M is the lateral mixing coefficient, Δx is the local grid spacing and Δx_m is its maxium value in the model domain. The horizontal mixing of temperature/salinity is parameterized by a Laplacian scheme along isopycnal levels with the eddy diffusivity denoted as A_H. Different values of A_M and A_H are used for the two models. CREG12 uses $A_M = 4 \times 10^9$ m^{4}s^{-1} and $A_H = 50$ m^{2}s^{-1}. For NEP36, simulation tests are carried out using different values of A_M and A_H. Figure 2 shows the time series of total kinetic energy (TKE) averaged over the NEP36 domain. For NEP36, the highest level of TKE, about 75% higher than the average value of TKE of CREG12, is obtained with $A_M = 10^8$ m^{4}s^{-1} and $A_H = 25$ m^{2}s^{-1}. Reducing A_H to 10 m^{2}s^{-1} causes a slight decrease of TKE. However, further reducing the value of A_M to 10^7 m^{4}s^{-1} causes a significant reduction of TKE to the level of CREG12. This reduction of TKE associated with decreasing A_M in certain range of values in NEMO v3.1 was first identified by Zhai *et al.* (2015) in analysis of the GBN36 model. They pointed that this model behavior is related to a numerical issue noted by Hollingsworth *et al.* (1983). In the following analysis, the NEP36 results are obtained using $A_M = 10^8$ m^{4}s^{-1} and $A_H = 25$ m^{2}s^{-1}.

With the final choices of horizontal mixing parameters, the TKE time series in Figure 2 suggest the rapid development of differences in the two model solutions during the first month of simulations. Since the difference is sufficiently significant for the purpose of evaluating the influence of model's horizontal resolution, in this study we compare the 1-year solutions of 2003 from the two models.
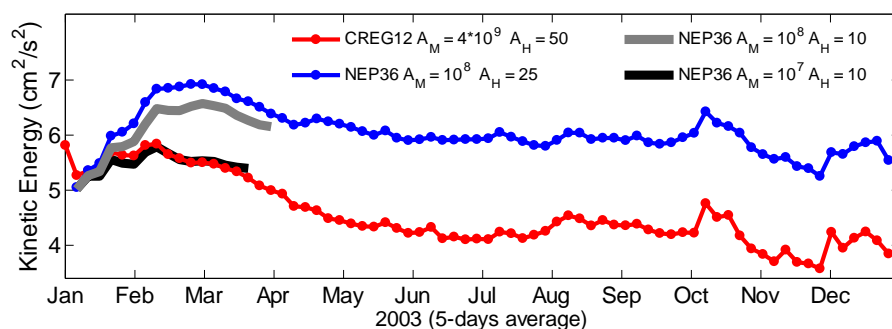

Figure 2. Time series of total kinetic energy averaged for the NEP36 region with water depth greater than 500 m, from a simulation with CREG12 (red curve) and three simulations of NEP036 (blue, gray and black curves). The values of horizontal eddy viscosity (A_M) and diffusivity for tracers (A_H) used for different simulations are denoted in the legend and discussed in the text.

3. Model Results

3.1 Sea Surface Height Variations

Meso-scale eddies contribute to a dominant part of ocean's kinetic energy on time scales of 20–150 days and spatial scales of 50–500 km. Eddy-induced sea level variations can be mostly captured by sea level anomalies (SLA) from satellite altimetry observations (Stammer, 1997; Fu *et al.*, 2010). Here we obtain the along-track altimeter data distributed by Archiving, Validation and Interpretation of Satellite Oceanographic data (AVISO, http://www.aviso.altim etry. fr/). The along-track SLA data have a nominal 10-day repeat cycle, and a horizontal along-track resolution of about 6.2 km. The SLA from the two models are obtained by applying a high-pass Butterworth filter to the 5-day averaged time series of sea level at each model grid, with a cut-off period of 90 days. The modelled SLA fields are then interpolated to the positions of altimeter tracks at the time close to altimeter observations.

Figure 3 shows the root mean squares (rms) and skewness of SLA from altimeter observation and the two models. For the rms plots, the color axis of altimeter data is increased by 0.02 m relative to that of the two models. Taking account of this shift, the spatial variations in the magnitude of SLA rms for the three sets of data are quite consistent. Also in reasonable agreement is the skewness of the SLA. In particular, off the shelf break in the northern part of the domain, the elevated rms and positive skewness are consistent with the observed and modelled eddy statistics reported by Crawford *et al.* (2000) and Stacey *et al.* (2006). In the interior basin the two models generally obtain larger skewness values than altimeter observations, possibly because the influence of noise in the altimeter data becomes relatively more significant in regions with weaker eddy activity.

Time series of SLA along a track nearly parallel to the coastline (denoted by bold pink in Figure 1) are shown in upper panels in Figure 4. The altimeter data contains an obvious component of noise, but stronger signals above the noise level show similarity with the results of the two models. It should be noted that without data assimilation the two models do not reproduce the observed timing and location of eddies. Instead, we expect the models to obtain similar statistics of SLA as the observations. The lower panels of Figure 4 compare the wavenumber spectra of SLA in variance-preserving form, computed for each track at a time (roughly every 10 days). First, models and observations show similar time variation of the wavenumber spectra over 2003, with the strongest spectral energy showing in January–February, and a secondary peak in July–September. The averaged spectra over the whole year, in both logarithmic and variance-preserving forms, are shown in Figure 5. The two models show very similar wavenumber spectra, with energy-containing band at wavelengths exceeding 100 km and the peak energy contribution occurs around 300 km. Note that wavelength in km equals to the inverse of wavenumber in c.p.km. NEP36 obtains slightly higher spectral energy than CREG12. The spectra of observational data show similar wavenumber distribution as the model results, but contain a component of noise. The level of white noise is estimated to be about 10^{-2} m^2 km according the spectral plot in logarithmic scale (Figure 5, left panel). Even with this estimation of spectral noise removed, the time-averaged spectral density is still higher than that obtained by the two models, primarily because the models under estimate the spectral density during the strong eddy events in January–February.
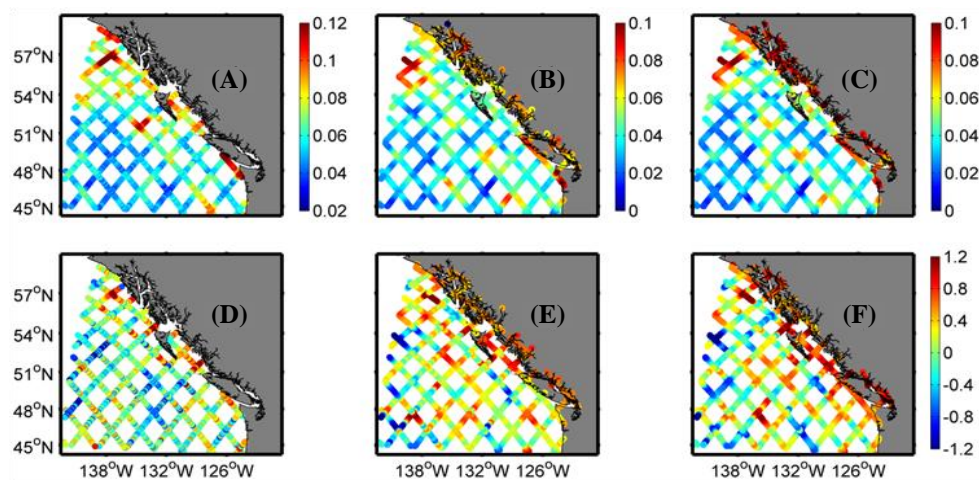

Figure 3. Upper row: Root mean square (in m) of SLA. Lower row: skewness of SLA. From left to right: along-track altimeter data (**A** and **D**), NEP36 (**B** and **E**), and GREG12 (**C** and **F**).
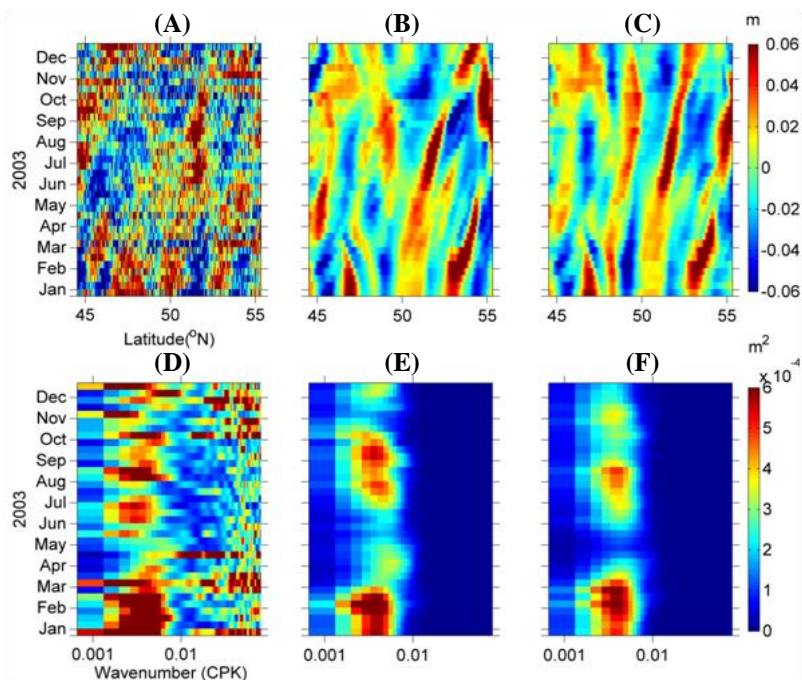
Figure 4. Upper row: Space-time variations of SLA (in m). Lower row: Time-variation of SLA wavenumber spectra in variance-preserving form (color shading in m²). All data shown are along the track highlighted in pink in Figure 1, and the spectra are computed for the segment between 44.5 °N and 55.5 °N. From left to right: along-track altimeter data (**A** and **D**), NEP36 (**B** and **E**), and GREG12 (**C** and **F**).
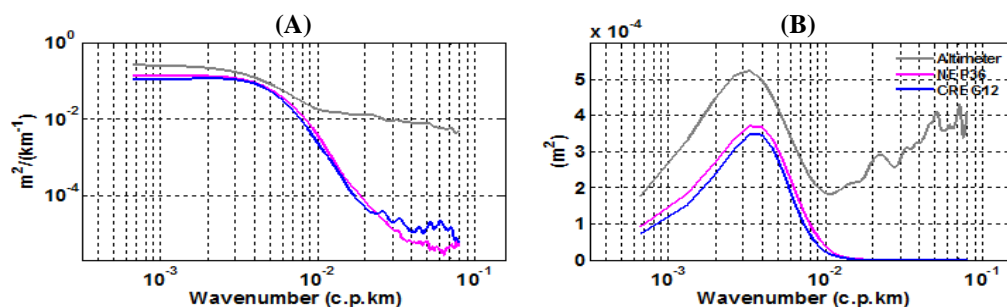

Figure 5. The time-averaged SLA wavenumber spectra shown in Figure 4, in (**A**) logarithmic spectral density and (**B**) variance-conserving form.

3.2 Sea Surface Current Variations

The energy of meso-scale eddies can also be quantified with the variations of sea surface current. While model outputs include total surface currents, here we examine the surface geostrophic currents for comparison with that derived from altimeter observations. Surface geostrophic currents are computed according to $u = -\frac{g}{f}\frac{\partial \eta}{\partial y}, v = \frac{g}{f}\frac{\partial \eta}{\partial x}$, where g is the gravitational acceleration, f is the Coriolis parameter, x and y are two horizontal coordinates, u and v are two components of velocity and η is SSH.

We first examine the time-mean currents. For model results, the mean surface geostrophic currents are computed from the time-mean SSH of both models. For observations, they are calculated based on the mean dynamic topography (MDT), namely the MDT_CNES-

CLS09 distributed by AVISO (Rio *et al.*, 2011). This gridded MDT product has a spatial resolution of about 30 km. The upper panels of Figure 6 show an overall agreement among the three sets of estimates. They all show strong currents in the northern region, while the two models show stronger currents in the interior basin of the southern region. In the southern interior basin both models exhibit stronger eddy-like features that are not presented in the MDT results. This discrepancy is possibly due to the model solutions are for one year only. The lower panels of Figure 6 present the time-mean total surface currents from the two models. The total currents have similar patterns but stronger speeds compared with the surface geostrophic currents. It is also notable that in deep waters of the southern part of the model domain, the zonal component of the total surface current from CREG12 is much stronger than that from NEP36.
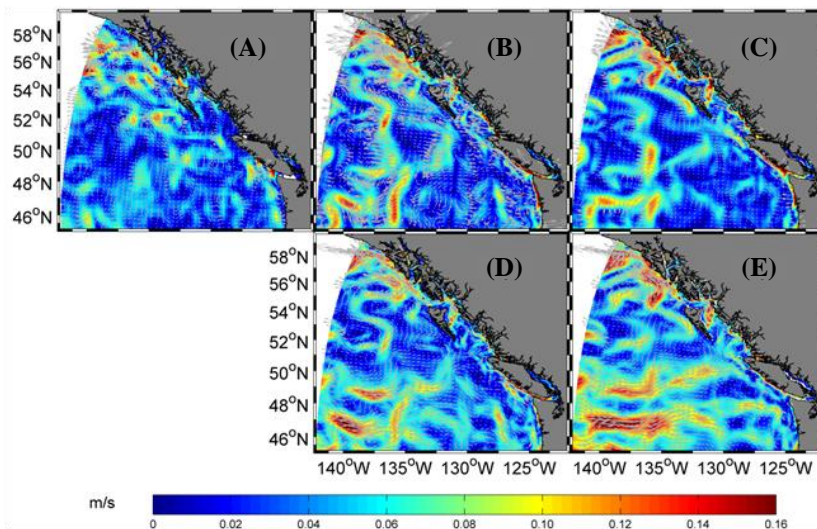
Figure 6. Upper row: Time-mean surface geostrophic currents. Lower row: Time-mean surface currents. From left to right: AVISO (**A**), NEP036 (**B** and **D**) and CREG012 (**C** and **E**). Color shading shows speed in ms^{-1}, and vectors show direction of currents.

Next we examine the eddy kinetic energy defined as $KE = (u'^2 + v'^2)/2$. For observations, the eddy components of surface geostrophic velocities, u' and v', are obtained from the gridded product of AVISO. For model results, u' and v' are computed from the SLA fields. For both observations and model results, a seasonal cycle for the velocity component at each location is removed, while the seasonal cycle is obtained by fitting an annual and a semi-annual harmonic to the time series. Further, a spatial low-pass Butterworth filter with a cutoff wavelength of 30 km is applied to u' and v' from AVISO and models. This filtering effectively removes the noise at smaller spatial scales. The resulting three estimates of EKE are shown in Figure 7. They all show elevated EKE near the shelf break from south to north, and from the shelf beak penetrating into the interior in the northern region. In the northern region, the area integral of EKE is the largest in AVISO, followed by NEP36 and then CREG12. In the southern region near the shelf break, the area integral of EKE is the largest in NEP36 but similar in AVISO and CREG12.

In the interior basin of the southern region, NEP36 obtains the highest EKE, followed by CREG12, and then AVISO.

Focusing on the interior basin of the southern region, we compute the wavenumber spectra of EKE over the box outlined in the lower panels of Figure 7. Figure 8 shows the resulting spectra in variance-preserving form, calculated for each 5-day averaged fields. From June to January, NEP36 obtains the highest spectral energy, followed by CREG12 and then AVISO. During February–May, NEP36 obtains the highest spectral energy, followed by AVISO and then CREG12. The time averages of these spectra, in both logarithmic and variance-preserving forms, are shown in Figure 9. For all three estimates, the energy-containing band presents at wavelengths exceeding 30 km and the peak energy contribution occurs around 130 km. Across the energy-containing band, CREG12 and AVISO obtain similar level of spectral energy, while being smaller than NEP36.
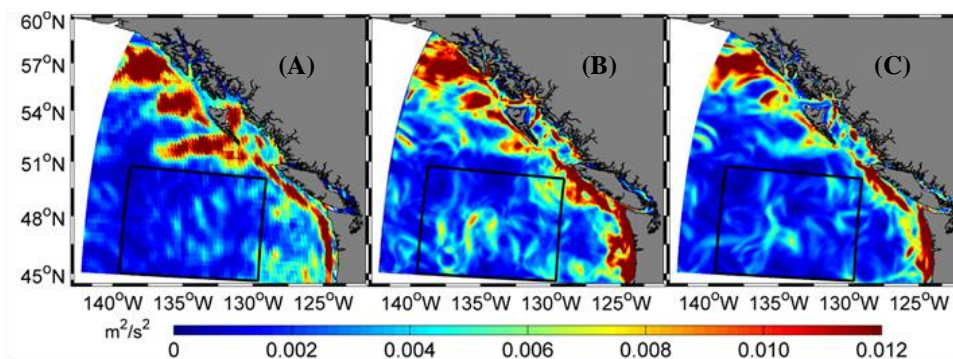

Figure 7. Eddy kinetic energy (lower row) (in m^{2}s^{-2}) for surface geostrophic currents. From left to right: gridded altimeter observation (**A**), NEP36 (**B**) and CREG12 (**C**). The box denotes the area for 2D spectral analysis.
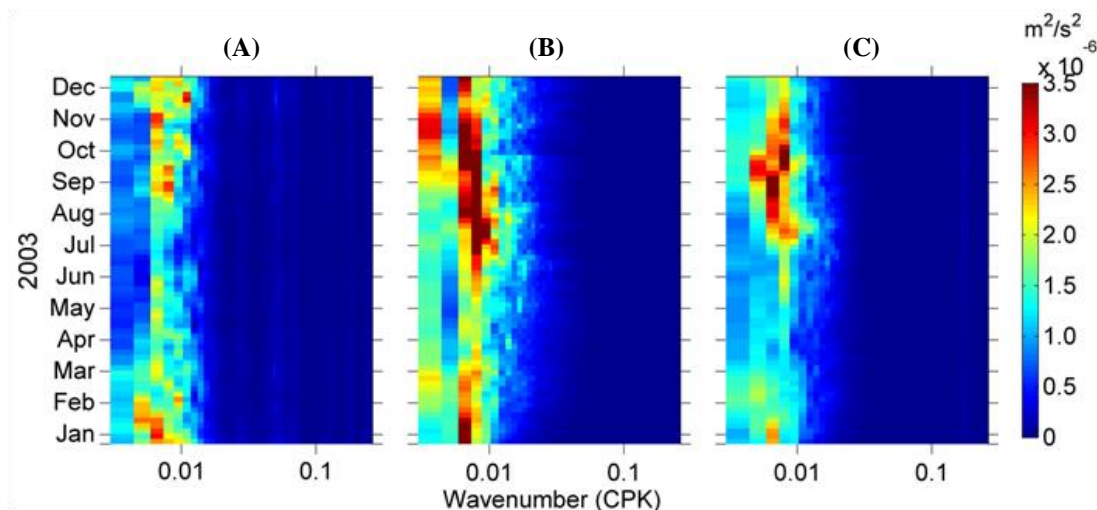
Figure 8. Time-variation of the 2D wavenumber spectra of EKE in variance-preserving form (color shading in m^{2}s^{-2}) calculated for data in the box shown in Figure 7. From left to right: based on gridded altimeter data (**A**), NEP36 (**B**), and GREG12 (**C**).
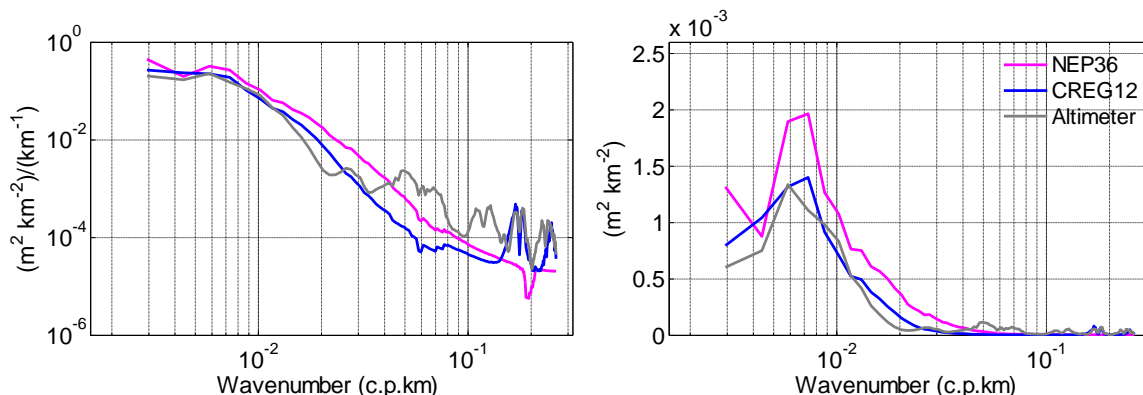

Figure 9. The time-averaged EKE 2D wavenumber spectra shown in Figure 8, in (left) logarithmic spectral density form and (right) variance-preserving form. Gray, pink and blue lines are based on gridded altimeter data, NEP36, and GREG12, respectively.

3.3 Ocean Temperature Variations

In order to compare the characteristics of ocean temperature variations from the two models, the whole-year time series from January to December 2003 are divided into four seasons, with a length of 3 months for each, denoted as winter, spring, summer and fall, respectively. Figure 10 shows the NEP36 solution of seasonal mean temperature from surface to 90 m depth, along a section from the west coast of Vancouver Island extending westward (bold black line in Figure 1). This section roughly follows a regular ship-board survey route named Line P (Crawford *et al.*, 2007). The CREG12 solution of seasonal mean temperature is very similar and hence is not shown. Clearly, in winter the upper ocean is weakly stratified with a thermocline appearing at 60–80 m depth. In spring the stratification starts to develop but is still weak. In summer strong stratification is developed with a thermocline located at 20–30 m depth. In autumn the strong stratification still

persists, and the thermocline is lowered to 30–40 m depth. This structure of seasonal-mean temperature influences the characteristics of temperature variations, with the most significant differences between the two model solutions appearing in the horizontal gradient of the temperature. Here we compute the rms of the horizontal gradient of temperature (denoted as $\partial T/\partial x$) for each season along the same close to Line P section. Top panels of Figure 11 show the rms of $\partial T/\partial x$ from NEP36. The smallest rms values are found in winter when the upper ocean stratification is weak. In spring the rms values increase as the stratification develops. Large rms values are found in summer and fall when strong stratification presents. In summer and fall, the depths at which large rms values are found are round the base of the seasonal mean upper mixed layer (Figure 10). The lower panels of Figure 11 present the rms values of $\partial T/\partial x$ derived from the solution of CREG12. Overall, NEP36 obtains larger rms values than CREG12, in particular in summer and fall.
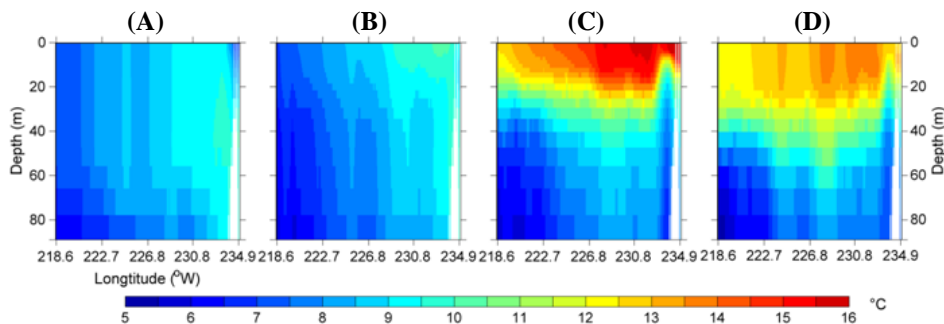
Figure 10. Seasonal mean temperature (in ℃) along the section highlighted in black in Figure 1, from the NEP36 simulation. From left to right: winter (**A**), spring (**B**), summer(**C**) and autumn (**D**).
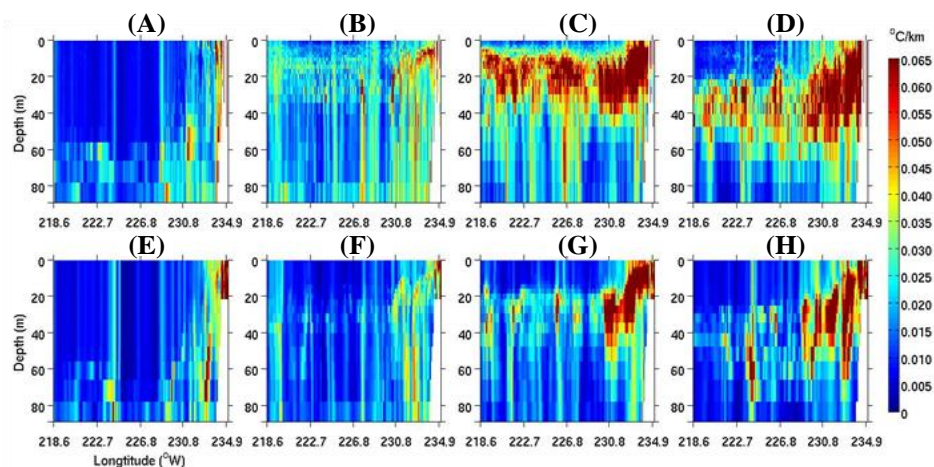

Figure 11. RMS of horizontal gradient of water temperature (in ℃ km^{-1}) along the section highlighted in black in Figure 1. Upper row: NEP36. Lower row: CREG12. From left to right: winter (**A** and **E**), spring (**B** and **F**), summer (**C** and **G**) and autumn (**D** and **H**).

Next, we compare the temperature variations from the two models at depth of 50 m. This depth is chosen because it is just below the seasonal mean depth of the upper mixed layer in summer and autumn, and where the seasonal differences in the rms of $\partial T/\partial x$ are obvious (Figure 11). Figure 12 shows that at this depth, the two models obtain very similar distribution of rms and skewness of temperature. The positive skewness near the shelf break in the northern part of the domain can be related to the energetic warm core eddies occurring there. The positive skewness in the interior basin of the southern region suggests that eddies in this region are also dominated by the warm core ones. Distinct differences between the two model solutions appear in the horizontal gradient of the temperature. Figure 13 shows snapshots of $((\partial T/\partial x)^2 + (\partial T/\partial y)^2)^{1/2}$, the magnitude of the horizontal gradient of temperature at 50 m depth, in four seasons. The two models show similar seasonal evolution and distribution. From winter to fall, the models resolve increasing eddy variations. In each season, NEP36 obtains more eddies with finer structure compared with CREG12.

Focusing on the interior basin of the southern region, we compute the wavenumber spectra for temperature at 50 m depth, and its horizontal gradient, respectively, over the box outlined in Figure 13 (A and E). Figure 14 shows the resulting spectra in variance-preserving form, calculated for each 5-day averaged fields. The two models obtain nearly the same spectra and their seasonal variations, with the strongest temperature variations occurring in fall, mainly October and November. The time averages of these spectra, in both logarithmic and variance-preserving forms, are shown in Figure 15. For temperature variations, the energy-containing band exists at wavelengths exceeding 20 km, and the energy contribution increases with the increasing wavelengths.

For the horizontal gradient of temperature, the two models show obvious differences. For NEP36, the energy-containing band exists at wavelengths exceeding 10 km, with the peak energy contribution occurring around 50 km. For CREG12, the energy-containing band exists at wavelengths exceeding 20 km, with the peak occurring around 70 km. Both models show strong variations of temperature gradient in fall, with a secondary peak in summer. Overall, NEP36 obtains a higher spectral level than CREG12.
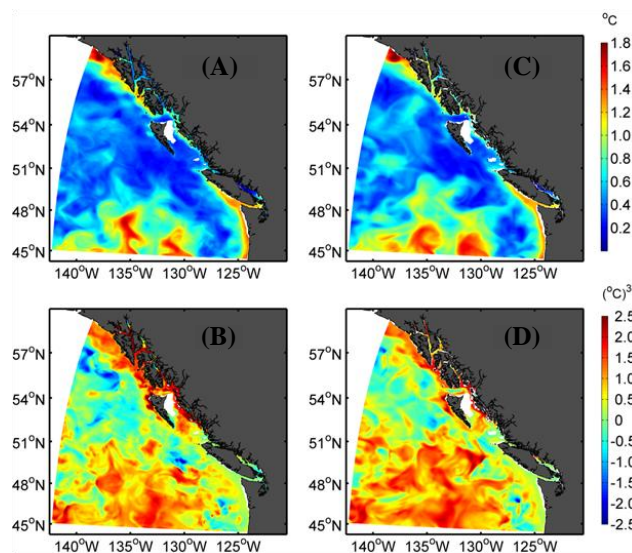
Figure 12. RMS (upper row, in °C) and skewness (low row, in (°C)^3) of temperature at 50 m derived from NEP36 (**A** and **B**) and CREG12 (**C** and **D**).
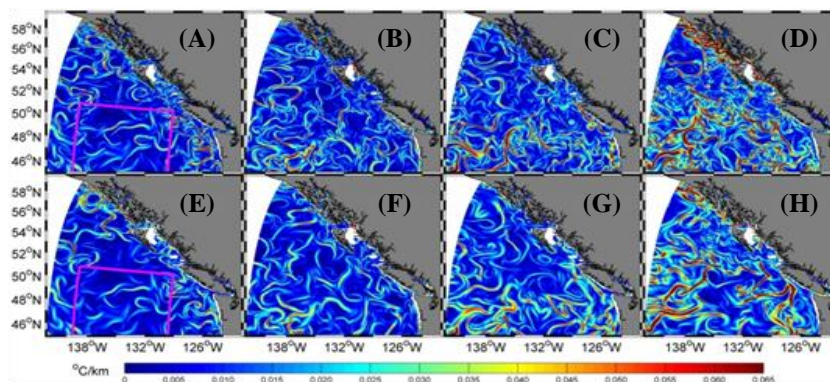

Figure 13. Snapshots of horizontal gradient of water temperature at 50 m depth (in °C km^{-1}) at 50 m. Upper row: NEP36. Lower row: CRE12. From left to right: winter (**A** and **E**), spring (**B** and **F**), summer (**C** and **G**) and autumn (**D** and **H**). The box outlined in **A** and **D** shows the area for 2D spectral analysis.
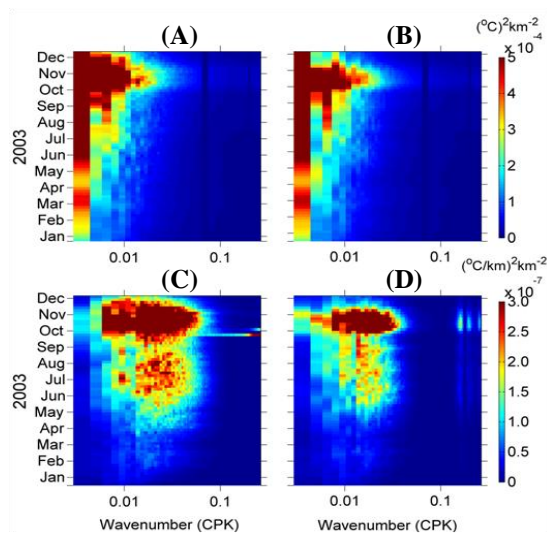

Figure 14. Time-variation of the 2D wavenumber spectra of (upper row) water temperature at 50 m depth and (lower row) its horizontal gradient, all in variance-preserving form. All are calculated for data in the box shown in Figure 12 (panels **A** and **D**). From left to right: NEP36 (**A** and **C**), and GREG12 (**B** and **D**).
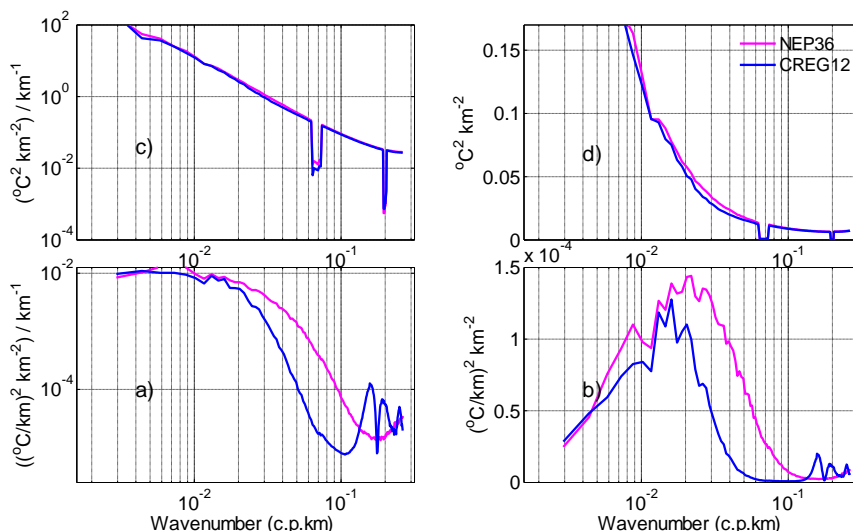
Figure 15. The time-averaged 2D wavenumber spectra shown in Figure 14, in (left) logarithmic spectral density and (right) variance-conserving form. Upper row: for water temperature. Lower row: for horizontal gradient of temperature. Pink and blue lines are for NEP36 and GREG12, respectively.

4. Conclusions and Discussions

The impact of horizontal resolution on meso-scale eddy simulations in the Northeast Pacific Ocean has been examined by using two ocean models (CREG12 and NEP36) at 7.5 km and 2.5 km resolution. The models are integrated for one year under realistic atmospheric and lateral forcing. Unlike the region around the Grand Banks of Newfoundland (GBN) where strong western boundary currents are present (*e.g*., Zhai *et al.*, 2015), the Northeast Pacific Ocean (NEP) features an eastern boundary current and a strong seasonal variation influenced by atmospheric forcing.

Similar with the results for GBN, in NEP the models produce sea level anomaly (SLA) variations similar with altimeter observations, in terms of rms, skewness and wavenumber spectra. The two models also obtain similar eddy characteristics of ocean temperature variations. The impacts of increasing model resolutions emerge in surface geostrophic currents and the horizontal gradient of temperature. Compared with CREG12, NEP36 obtains higher spectral energy for the EKE of surface geostrophic currents and for the horizontal gradient of temperature.

The energy-containing bands of wavenumbers in the spectra differ for different variables. Altimeter data and the two models obtain consistent results regarding the wavelengths at which the peak energy contribution in the spectra occurs: around 300 km for SLA and around 130 km for the EKE. For the spectra of water temperature, the two models show increase in energy contribution with the increasing wavelength, *i.e*., no peak is identified in the resolved range of wavelengths. For the spectra of

the horizontal gradient of temperature, the peak energy contribution occurs around 50 km in NEP36 and 70 km in CREG12. As both the energy-containing band and the peak energy contribution shift to shorter wavelengths, the NEP36 configuration obtains more spectral energy than the lower-resolution CREG12. The difference between the two model solutions in the spectra of horizontal gradient of temperature may be related to difference in the eddy-induced cascading processes to be examined in future studies.

The two models obtain similar seasonal variations of the spectra of the variables examined. For SLA, the highest spectral energy occurs in January–February, with a secondary peak in July–September. Note that the SLA spectra are computed along a line almost parallel to the coastline off the shelf break, hence the time-evolution of the SLA spectra may mainly represent the variations associated with the propagation of eddies. The spectra for other variables are computed for the interior basin of the southern region. For the EKE of surface geostrophic currents, higher spectral energy occurs from June to January than during February–May. For temperature, the highest spectral energy occurs in October–November. For the horizontal gradient of temperature, the highest spectral energy occurs in October–November, with a secondary peak during June–September. Clearly, there exists a degree of consistency in terms of the seasonal variations of eddies in this region in terms of surface geostrophic currents, temperature and its horizontal gradient. Understanding the forcing mechanism of the seasonal evolution of meso-scale eddies is an interesting topic for future studies.

One limitation of the present study is the length of model simulations, as 1-year time series do not allow robust separation of eddies from the mean state. Hence, multi-year simulations need to be carried out. The model evaluation is also limited by the use of satellite altimetry data, whether in gridded or along-track formats. For example, while CREG12 obtains the EKE spectra closer to altimeter observations than NEP36, we suspect that the spectral energy may be underestimated by the gridded altimeter data. Clearly, challenges remain in obtaining suitable observational data for the evaluation of high-resolution model solutions.

Conflicts of Interest

Acknowledgments

References

Axell L B. (2002). Wind-driven internal waves and Langmuir circulations in a numerical ocean model of the southern Baltic Sea. *Journal of Geophysical Research*, 107(11): 3204.
http://dx.doi.org/10.1029/2001JC000922

Amante C and Eakins B W. (2009). ETOPO1 1 arc-minute global relief model: Procedures, data sources and analysis. *Technical Report*. NOAA Technical Memorandum NESDIS NGDC-24. National Geophysical Data Center, NOAA.
http://dx.doi.org/10.7289/V5C8276M

Becker J J, Sandwell D T, Smith W H F, *et al*. (2009). Global bathymetry and elevation data at 30 arc seconds resolution: SRTM30_PLUS. *Marine Geodesy*, 32(4): 355-371.
http://dx.doi.org/10.1080/01490410903297766

Blanke B and Delecluse P. (1993). Variability of the tropical Atlantic ocean simulated by a general circulation model with two different mixed layer physics. *Journal of Physical Oceanography*, 23: 1363–1388.
http://dx.doi.org/10.1175/15200485(1993)023<1363:VOTTAO>2.0.CO;2

Crawford W R, Cherniawsky J Y and Foreman M G G. (2000) Multi-year meanders and eddies in the Alaskan Stream as observed by TOPEX/Poseidon altimeter. *Geophysical Research Letters*, 27(7): 1025–1028.
http://dx.doi.org/10.1029/1999GL002399

Crawford W, Galbraith J and Bolingbroke N. (2007). Line P ocean temperature and salinity, 1956–2005. *Progress in Oceanography*, 75(2): 161–178.
http://dx.doi.org/10.1016/j.pocean.2007.08.017.

Delworth T L, Rosati A and Anderson W. (2012). Simulated climate and climate change in the GFDL CM2.5 high-resolution coupled climate model. *Journal Climate*, 25: 2755–2781.
http://dx.doi.org/10.1175/JCLI-D-11-00316.1

Drakkar Group. (2007). Eddy permitting ocean circulation hindcasts of past decades. *CLIVAR Exchanges*, 12: 8–10.

Dupont F, Higginson S, Bourdallé-Badie R, *et al*. (2015). A high-resolution ocean and sea-ice modelling system for the Arctic and North Atlantic Oceans. *Geoscientific Model Development*, 8: 1577–1594.
http://dx.doi.org/10.5194/gmd-8-1577-2015

Ferry N, Parent L, Garric G, *et al*. (2012). GLORYS2V1 global ocean reanalysis of the altimetric era (1992–2009) at meso scale. *Mercator Quarterly Newsletter*, 44: 29–39.
http://www.mercator-ocean.fr/eng/actualites-agenda/newsletter, 2012.

Flather R A. (1976). A tidal model of the Northeast Pacific. *Atmosphere-Ocean*, 23: 22–45.

Fu L L, Chelton D B, Le Traon P Y, *et al*. (2010). Eddy dynamics from satellite altimetry. *Oceanography*, 23(4): 14–25.
http://dx.doi.org/10.5670/oceanog.2010.02

Gaspar P, Grégoris Y and Lefevre J M. (1990). A simple eddy kinetic energy model for simulations of the oceanic vertical mixing: Tests at station Papa and long-term upper ocean study site. *Journal of Geophysical Research*, 95(C9): 16179–16193.
http://dx.doi.org/10.1029/JC095iC09p16179

Hollingsworth A, Kalbers P, Renner V, *et al*. (1983). An internal symmetric computational instability. *Quarterly Journal of the Royal Meteorological Society*, 109(460): 417–428.
http://dx.doi.org/10.1002/qj.49710946012

Katavouta A, Thompson K R, Lu Y, *et al*. (2016). Interaction between the tidal and seasonal variability of the Gulf of Maine and Scotian shelf region. *Journal of Physical Oceanography*, 46: 3279–3298.
http://dx.doi.org/10.1175/JPO-D-15-0091.1

Madec G, Delecluse P, Imbard M, *et al*. (1998). OPA8.1 Ocean general Circulation Model reference manual. *Note du Pole de modelisazion*, Institut Pierre-Simon Laplace (IPSL), France, 11.

Madec G. (2008). NEMO ocean engine. *Note du Pole de modélisation*. No 27 ISSN No 1288–1619. Institut Pierre–Simon Laplace (IPSL), France.

Marchesiello P, McWilliams J C and Shchepetkin A. (2001). Open boundary conditions for long-term integration of regional oceanic models. *Ocean Modelling*, 3: 1–20.
http://dx.doi.org/10.1016/S1463-5003(00)00013-5

Mellor G and Blumberg A. (2004). Wave breaking and ocean surface layer thermal response. *Journal of Physical Oceanography*, 34: 693–698. http://dx.doi.org/10.1175/2517.1

Rio M H, Guinehut S and Larnicol G. (2011). New CNES-CLS09 global mean dynamic topography computed from the combination of GRACE data, altimetry, and *in situ* measurements. *Journal of Geophysical Research,* 116(7): http://dx.doi.org/10.1029/2010JC006505

Smith G C, Roy F, Mann P, *et al*. (2013). A new atmospheric dataset for forcing ice–ocean models: Evaluation of reforecasts using the Canadian global deterministic prediction system. *Quarterly Journal of the Royal Meteorological Society*, 140(680): 881–894. http://dx.doi.org/10.1002/qj.2194

Smith R D, Maltrud M E, Bryan F O, *et al*. (2000). Numerical Simulation of the North Atlantic Ocean at 1/10°. *Journal of Physical Oceanography*, 30: 1532–1561.

http://dx.doi.org/10.1175/1520-0485(2000)030<1532:NSOTNA >2.0.CO;2

Stacey M W, Shore J, Wright D G, *et al*. (2006). Modeling events of sea-surface variability using spectral nudging in an eddy permitting model of the northeast Pacific Ocean. *Journal of Geophysical Research*, 111: C06037. http://dx.doi.org/10.1029/2005JC003278

Stammer D. (1997). Global characteristics of ocean variability estimated from regional TOPEX/POSEIDON altimeter measurements. *Journal of Physical Oceanography*, 27: 1743–1769.
http://dx.doi.org/10.1175/1520-0485(1997)027<1743:GCOOVE>2.0.CO;2

Zhai L, Lu Y, Higginson S, *et al*. (2015). High-resolution modelling of the mean flow and meso-scale eddy variablity around the Grand Banks of Newfoundland. *Ocean Dynamics*, 65(6): 877–887. http://dx.doi.org/10.1007/s10236-015-0839-5